Seismic design and behavior of post-tensioned steel connections including effects of a composite slab

Chung-Che Chou [*], Yu-Chi Wang, Jun-Hen Chen

Department of Civil Engineering, National Chiao Tung University, Hsinchu, Taiwan

ARTICLE INFO

ABSTRACT

Three series of six full-scale, cyclic tests on post-tensioned (PT) beam-to-column connections were conducted to evaluate the cyclic performance. Each specimen represented an interior connection with steel beams PT to a column; one specimen also incorporated a composite slab. Reduced Flange Plates (RFPs) were added at the beam-to-column interface for energy dissipation, and flange reinforcing plates were provided outside the beam flanges to minimize yielding upon decompression. This paper describes the durability of the proposed connection, the effects of web stiffeners on beam local buckling, and the interaction of a composite slab. The first test series demonstrated that as long as beam yielding could be prevented before an interstory drift of 4%, the PT connection was capable of reaching an interstory drift of 5% or experiencing the AISC seismic loads twice without beam buckling. The second test series showed that beam buckling could be prevented by utilizing web stiffeners instead of increasing the length of the flange reinforcing plate. The third test series included a matched pair of specimens, one bare steel beam and one including a composite slab. Results that emphasize the influence of the composite slab on re-centering behavior and specific comments on the slab response were presented. The presence of a composite slab corresponded to higher-achieved moments due to the tensile capacities of the metal deck flutes, wire mesh, and longitudinal reinforcement, which were placed parallel to the PT beam. However, the re-centering behavior could be maintained after fractures of the wire mesh in the proposed slab details. Estimates of beam moments considering the presence of a composite slab were presented based on the cyclic test results.

1. Introduction

The widespread damage observed at welded moment connections after the Northridge and Kobe earthquakes initiated extensive research aimed at improving the cyclic behavior. Connections characterized by either strengthened or reduced flexural capacity of the beam near the column face [1–3] have been demonstrated to develop ductile seismic response. However, these moment connections are vulnerable to residual drift, which might cause discomfort for occupants after earthquakes. Researchers [4–7] have developed alternative steel post-tensioned (PT) connections for seismic use in moment-resisting frames. Ricles et al. [4] utilized PT strands as the re-centering element and angles as the energy-dissipating element in steel PT connections. The re-centering responses of the PT connections were verified from tests. Garlock et al. [5] investigated several performance limit states of the PT connections with a larger beam size than that in Ricles et al. [4]. Christopoulos et al. [6] employed a sectional analysis to predict a monotonic moment gap-opening angle relationship of a PT connection with PT bars and restrained reinforcing bars. The proposed numerical model closely predicted the cyclic responses of the PT connection. Chou et al. [7] studied the PT connections with reduced flange plates (RFPs) as energy dissipators, and utilized a non-linear finite element analysis to explore the stress-disturbed region in the PT beam. The test results clearly showed the need for restraining devices for the RFPs in dissipating energy in compression; therefore, the restraining device is included but modified in the present study to prevent RFP buckling. Furthermore, the prior study [7] utilized the PT beams with an insufficient length of the flange reinforcing plate, leading to beam local buckling at a 4% drift. This study evaluates the effects of the flange reinforcing plate length and a pair of web stiffeners in preventing beam local buckling [8]. Chou et al. [9] also tested one PT connection specimen with a composite slab. The composite slab, following steel construction practice in Taiwan, had the metal deck flutes, longitudinal reinforcement, and welded wire mesh placed parallel to the PT beams. For the beam under negative bending, the test results showed significant residual deformation and no re-centering response due to tensile capacity of the slab. To reduce a composite slab restraint in the PT connection, additional speci-

* Corresponding author. Tel.: +886 3 571 2121x54961; fax: +886 3 571 6257.
E-mail address: chchou@mail.nctu.edu.tw (C.-C. Chou).

(a) PT connection.
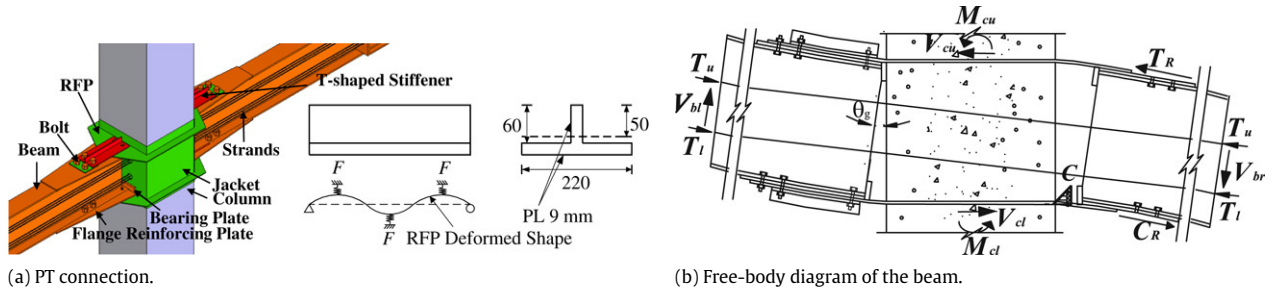
(b) Free-body diagram of the beam.

Fig. 1. PT connection with RFPs restrained by T-shaped stiffeners instead of flat plates.

mens are prepared in this study with different top and bottom RFPs and different slab details [10].

The objectives of this research investigated (1) durability of the PT connection designed based on the beam axial force and moment at the gap-opening angle of 0.03 rad. (approximately 4% drift), (2) whether beam local buckling could be prevented by adding web stiffeners near termination of the flange reinforcing plate, and (3) interaction of a composite slab. A total of six PT connection subassemblies were planned and tested for fulfilling these objectives. The first five tests were on bare steel beam specimens. The last two specimens were identical, but the addition of a composite slab was included in only one specimen. The interaction of the composite slab on the PT connection behavior could be investigated.

2. Post-tensioned connection behavior

The proposed PT connection [Fig. 1(a)] includes a reinforced concrete column, two steel beams, top and bottom RFPs, and seven wire, ASTM A416 Grade 270 strands running along the beam web and anchored at both ends of the beams. Flange reinforcing plates are welded outside the beam flanges to minimize yielding upon decompression, and bearing plates are placed between the column and beam to avoid bearing failure of the concrete in the panel zone. For easy construction, the connection uses a steel jacket instead of transverse reinforcement to confine concrete. The RFPs, designed based on the procedure in Chou et al. [7], are shop-welded along the perimeter of the jacket and then bolted to the beam flanges in the field. The prior study [7] showed that although the RFP was restrained by a flat plate, it still buckled due to insufficient restraint. A T-shaped stiffener instead of a flat plate is proposed in this study to enhance out-of-plane restraint. The T-shaped stiffener is designed as a simply-supported member between bolts at both ends. A deformed RFP, observed in the previous test when the RFP buckling occurred, is used to estimate the spring force, F, acting to the stiffener. Allowing a 1 mm deformation in the spring, the spring force is determined based on the study by Timoshenko and Gere [11]. The size of the T-shaped stiffener is determined to ensure the extreme fiber flexural stress less than the yield strength of the steel.

A simplified analysis of the behavior for the PT connection without a composite slab can be explained using the free-body diagram shown in Fig. 1(b). The PT connection behaves as a fully restrained moment connection provided the beam moment is less than the decompression moment, M_d, at the beam-to-column interface:

$$M_d = M_{d,ST} + M_{d,R}$$
$$= \left[T_{in} \left(\frac{d_b}{2} - t_f \right) \right] + \left[T_R \left(d_b + 2t_p + t_R \right) \right] \tag{1}$$

where $M_{d,ST}$ and $M_{d,R}$ are the moments provided by the initial strand force, T_{in}, and the RFPs, respectively; T_R is the tensile force in the

RFP; t_R is the thickness of the RFP; t_p is the thickness of the flange reinforcing plate; t_f is the thickness of the beam flange, and d_b is the beam depth. After the beam moment is greater than the decompression moment, a gap develops at the beam-to-column interface. The moment, M_b, developed in the PT connection for a gap-opening angle, θ_g, is:

$$M_b = M_{ST} + M_R$$
$$= \left[T_{ST} \left(\frac{d_b}{2} - t_f \right) \right] + \left[T_R \left(d_b + \frac{t_R}{2} + t_p - t_f \right) \right.$$
$$\left. + C_R \left(\frac{t_R}{2} + t_p + t_f \right) \right] \tag{2}$$

where M_{ST} and M_R are the moments provided by the strands and the RFPs, respectively, and C_R is the compressive force in the RFP. Eqs. (1) and (2) are proposed in this study for simplicity, but the prediction errors according to closed-form expressions in the prior study [7] are minimal. Considering strand elongation and beam shortening following decompression, the total strand force, T_{ST}, which equals the summation of the upper and lower strand forces T_u and T_l, can be estimated. The tensile force, T_R, and compressive force, C_R, in the RFPs can also be estimated from deformation between the column face and the beam flange-RFP joint, and the axial force-deformation relationship of the RFP. The iterative beam sectional analysis [7] can be adopted to determine the strand force, RFP force, and beam moment.

3. Test specimens

The experimental program consisted of tests of six full-scale specimens. The first five specimens included steel PT beams (H500 × 200 × 10 × 16), a reinforced concrete column (650 × 650), and RFPs. Specimen 6 was identical to Specimen 5, but had the addition of a composite slab. Typical connection details are shown in Fig. 2(a); Specimens 1, 2, 5, and 6 used a steel jacket instead of transverse reinforcement to confine the concrete in the connection. Specimens 3 and 4 did not use a steel jacket; transverse reinforcement, as specified in Section 21.4 of ACI 318 [12], was provided in the connection. For Specimen 4 shown in Fig. 2(b), the RFPs were first welded to the bearing plates and then bolted to the beam flanges in the shop. After the beams were post-tensioned to the column, the bearing plates were bolted to the column. All columns and panel zones were designed to remain elastic.

A summary of the RFP sizes is given in Table 1. Specimens 1, 2, and 4 used 8 mm thick top and bottom RFPs. To increase energy dissipation of the connection, Specimen 3 had 12 mm thick top and bottom RFPs. Specimen 5 had an 8 mm thick bottom RFP and a 4 mm thick top RFP in order to match Specimen 6, which also had a 150 mm thick normal-weight concrete slab (Fig. 3). The existing slab details for typical steel moment-resisting frames in Taiwan include: (1) a metal deck is 1.2 mm thick, continuously placed with 75 mm deep flutes running parallel to the moment connections, (2) a #3 longitudinal bar is continuously placed inside each flute, and
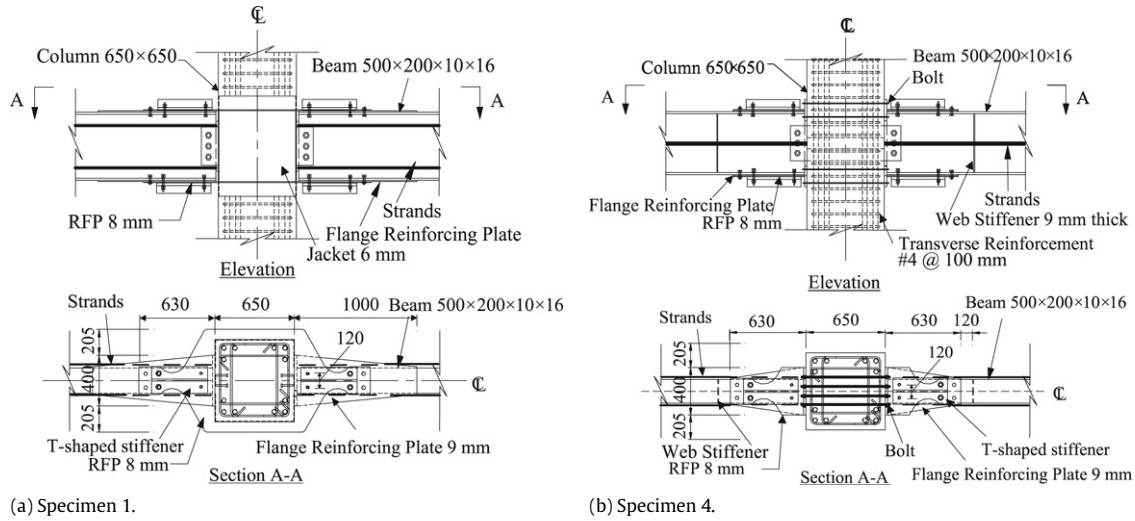
(a) Specimen 1. (b) Specimen 4.

Fig. 2. Specimens 1 and 4 connection details (unit: mm).

Table 1
Design parameters

Specimen No.	1	2	3	4	5	6
t_R (mm) Top	8	8	12	8	4	4
t_R (mm) Bottom	8	8	12	8	8	8
θ_{sg} (rad.)	0.03	0.03	0.01	0.01	0.03	0.03
L_R	$1.5d_b$	$2d_b$	$1.5d_b$	$1.25d_b$	$2d_b$	$2d_b$
t_j [a] (mm)	6	6	–	–	6	6
Number of strands	14	16	16	14	16	16
T_{in} (kN)	971	957	1203	957	975	940
M_d/M_{np}	0.39	0.39	0.50	0.39	–	–
$M_{0.03}$ [b] $/M_{np}$ [c]	0.80	0.85	1.02	0.80	–	–

[a] Jacket plate thickness.
[b] Beam moment at the gap-opening angle of 0.03 rad.
[c] Nominal moment capacity (=723 kN m).

(3) top reinforcement is limited to a 100×100 mm welded wire mesh for controlling concrete shrinkage. The developed slab details were identical to the existing slab details, except that the metal deck was discontinuous at the column centerline and longitudinal bars had a 2000 mm debonded length near the connection to minimize a restraint during opening of the gap at the beam-to-column interface [Fig. 3 (d)]. In addition, the cross-sectional area of the top RFP plus longitudinal bars was close to that of the bottom RFP to provide similar positive and negative beam moments. A 25 mm-gap between the column and the concrete slab was also provided to prevent the slab from bearing on the column. Nelson headed shear studs of 120 mm long, 22 mm in diameter, were fillet welded 132 mm on center to the beam top flange to provide full composite action. The composite specimen had similar details as the one tested by Chou et al. [9], except that the previous composite specimen had metal deck flutes running through the column centerline and had the same thickness of the top and bottom RFPs.

By considering the axial force and bending moment in the beam, the length of the flange reinforcing plate, L_R, was determined to limit the beam flange strain (where the flange reinforcing plates terminate in the beam) to the yield strain at a specified gap-opening angle, θ_{sg}:

$$L_R = L_b - \frac{2I_b}{V_b d_b}\left(\phi_b \sigma_y - \frac{T_{ST}}{A_b}\right) \tag{3}$$

where L_b is the distance from the actuator to the column face; A_b is the beam cross sectional area; I_b is the moment inertia of the beam; V_b is the beam shear; σ_y is the yield strength of the steel, and ϕ_b (=0.9) is the safety reduction factor. The angle values of 0.02

and 0.03 rad. were, respectively, adopted in the prior research [7] and in this study for Specimens 1, 2, 5, and 6 (Table 1). The lengths of the flange reinforcing plates for Specimens 3 and 4, however, were determined based on the beam axial force and moment at the gap-opening angle of 0.01 rad. The objective of using different gap-opening angles to determine the length of the flange reinforcing plate was to investigate the effects of the plate length on the PT connection cyclic responses. Selecting a gap-opening angle of 0.01 rad. in the present study evaluated the flange strain when beam local buckling occurred. This strain could be compared with that obtained in the previous study [7], which used a gap-opening angle of 0.02 rad. to determine the plate length. Selecting a gap-opening angle of 0.03 rad. in the present study could ensure that beam local buckling be avoided at the ultimate response. Because the initial PT force, the number of strands, and the size of the RFPs in Specimen 4 were smaller than those in Specimen 3, Specimen 4 had shorter flange reinforcing plates (Table 1).

When the beam flange near the end of the flange reinforcing plate reached 1.4 times the yield strain, indicating the onset of beam local buckling [7], the gap-opening angles were about 0.03 rad. ($\approx 4\%$ drift) for Specimens 3 and 4. Table 2 lists values calculated based on the moment-axial compression interaction equation at beam sections where the flange reinforcing plates are terminated:

$$\frac{P_u}{\phi_b P_y} + \frac{M_u}{\phi_b M_y} \tag{4}$$

where P_u ($=-T_{ST}$) is the PT force at a 4% drift; M_u is the moment at a 4% drift; P_y is the yield strength of the beam, and M_y is the yield moment of the beam. Note that Specimens 1 and 2 have values less than 1, indicating that the beam section at this location is able to resist both the PT force and moment. However, Specimens 3 and 4 have values larger than 1, indicating that the web stiffeners are required to prevent beam local buckling. For comparison purposes, two full-depth web stiffeners were introduced in Specimen 4 [Fig. 2(b)] at a likely location of beam local buckling observed from the prior test [7]. The distance between the end of the flange reinforcing plate and the web stiffener was a quarter of the beam depth, which was adopted based on a possible plastic hinge location in the cover plated moment connection [13]. The thickness of the web stiffener (9 mm) was selected to be close to that of the beam web (10 mm).

Table 3 provides yield stress, F_y, and tensile strength, F_u, for the steel materials used in the specimens. The material properties were obtained by testing tensile coupons in accordance with ASTM
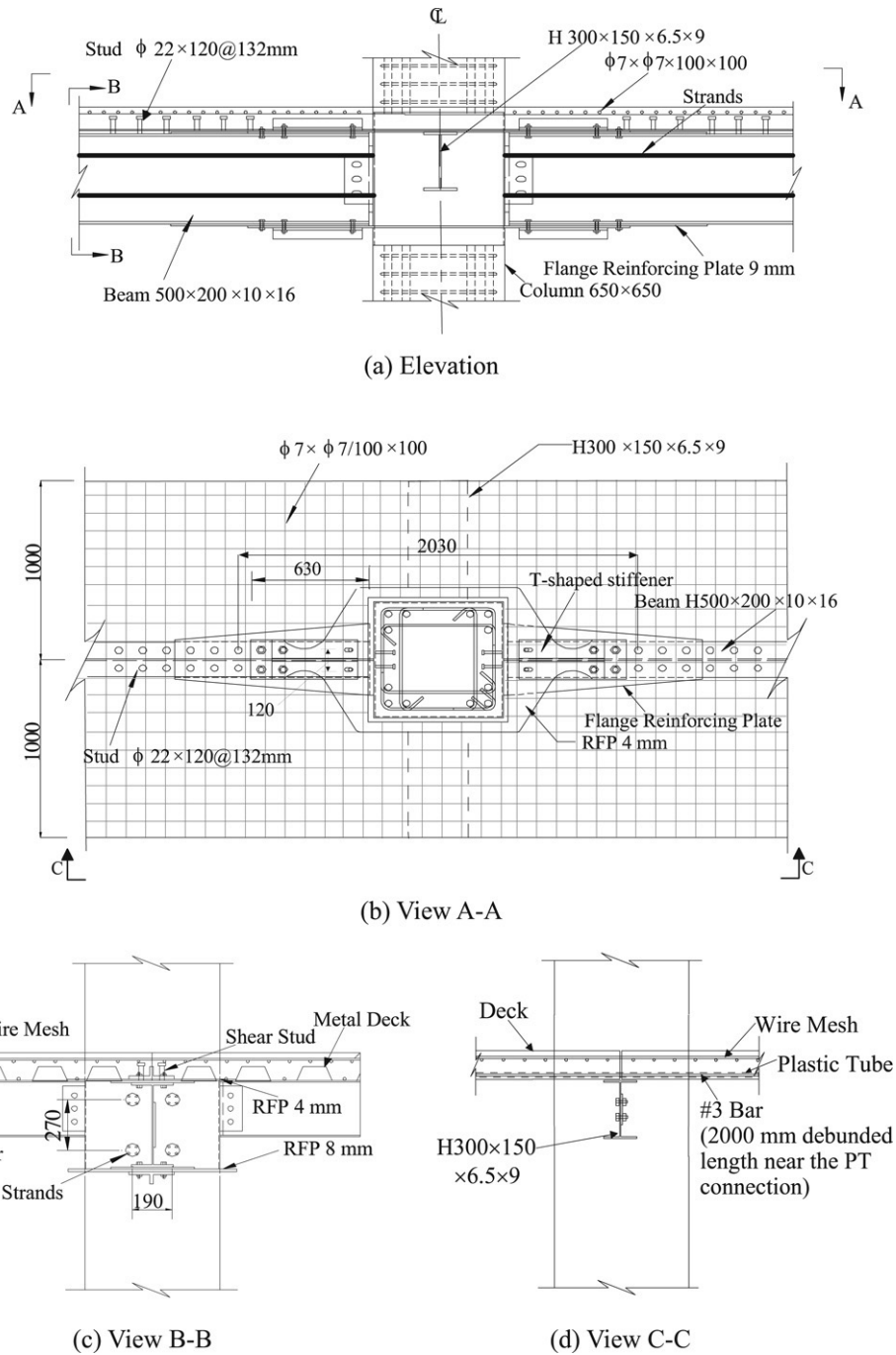
(a) Elevation

(b) View A-A

(c) View B-B   (d) View C-C

Fig. 3. Specimen 6 details (unit: mm).

Table 2
Moment-axial compression interaction values

Specimen no.	L_R (d_b)	$\frac{P_u}{\phi_b P_y}$		$\frac{M_u}{\phi_b M_y}$		Combined value		Web stiffeners	Beam local buckling in test
		Ana.[b]	Exp.[c]	Ana.	Exp.	Ana.	Exp.		
1	1.5	0.39	0.36	0.58	0.62	0.97	0.98	No	No
2	2	0.40	0.38	0.51	0.56	0.91	0.94	No	No
3	1.5	0.47	0.43	0.73	0.72	1.20	1.15	No	Yes
4	1.25	0.38	0.34	0.65	0.76	1.03	1.10	Yes	No
CFT[a]	1.5	0.48	0.47	0.63	0.65	1.13	1.14	No	Yes

[a] Obtained from Specimen 3 in Chou et al. [7].
[b] Computed based on the predicted PT force and moment.
[c] Computed based on the experimental PT force and moment.

Table 3
Steel material strengths

Strength	Beam		RFP				Wire mesh	#3 Bar	Metal deck
	Web	Flange	4 mm (SS 400)	8 mm (A36)	8 mm (SS 400)	12 mm (A36)			
F_y (MPa)	400	393	301	324	316	290	339	356	249
F_u (MPa)	517	496	418	441	411	434	470	480	294
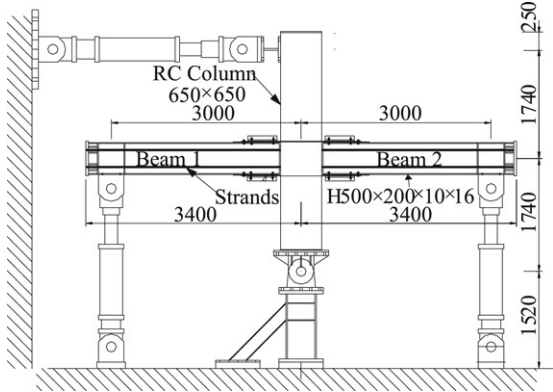
Fig. 4. Test setup (composite slab not included).

standards [14]. Note that ASTM A36 steel was used for the RFPs of Specimens 1 through 4, and SS400 steel was specified for the RFPs of Specimens 5 and 6. The compressive strength of the normal-weight concrete in the composite slab was 29 MPa at day of testing.

4. Test setup and results

4.1. Test setup

Each specimen was tested in the setup (Fig. 4) by displacing actuators at both ends of the beams via a series of displacement cycles, consistent with the AISC loading protocol [15]. The test instrumentation included: load cells to monitor the force in each post-tensioning strand, displacement transducers to monitor the gap opening at the beam-to-column interface, and strain gauges to measure strain in the beam, reinforcement, wire mesh, and

deck. Each specimen was painted prior to testing to provide visual evidence of yielding.

4.2. Test results

Fig. 5 shows the specimen responses. The moment was calculated by the applied lateral load times the distance from the actuator to the column face. The decompression moment was reached beyond an interstory drift of 0.5%, followed by a decrease in the subassembly stiffness. The measured moments at decompression or at the gap opening angle of 0.03 rad. (Table 4) are generally higher than the predicted values (Table 1). Eqs. (1) and (2) are, therefore, slightly conservative. The gap opening angle, θ_g, was measured using a set of displacement transducers at the beam-to-column interface (using their difference between the two measurements divided by their distance). Details of specimen responses are described below.

4.2.1. Specimens 1 and 2

With the same RFPs and similar initial PT forces (Table 1), Fig. 5(a) and (b) show that Specimen 2 has a higher post-yielding stiffness and moment after decompression than Specimen 1 due to the number of strands (see Table 1). Beam yielding was not observed at an interstory drift of 4% due to an adequate length of the flange reinforcing plate. For Specimen 1 loaded to an interstory drift of 5%, minor yielding in the beam web and flange, as expected, was observed [Fig. 6(a)]. The maximum beam moment was 0.92 M_{np}, and a reduction in the negative moment was due to a fracture of one RFP in tension. Specimen 2, instead of being loaded to an interstory drift of 5%, was tested twice using the same AISC loading protocol [15] to examine the connection durability. The two tests had quite similar hysteretic behaviors [Fig. 5(b)] before the RFP fractured toward the second cycle of −4% drift [Fig. 6(b)]. The RFP fracture was not observed in the prior research [7].

(a) Specimen 1.

(b) Specimen 2.

(c) Specimen 3.

(d) Specimen 4.

(e) Specimen 5.
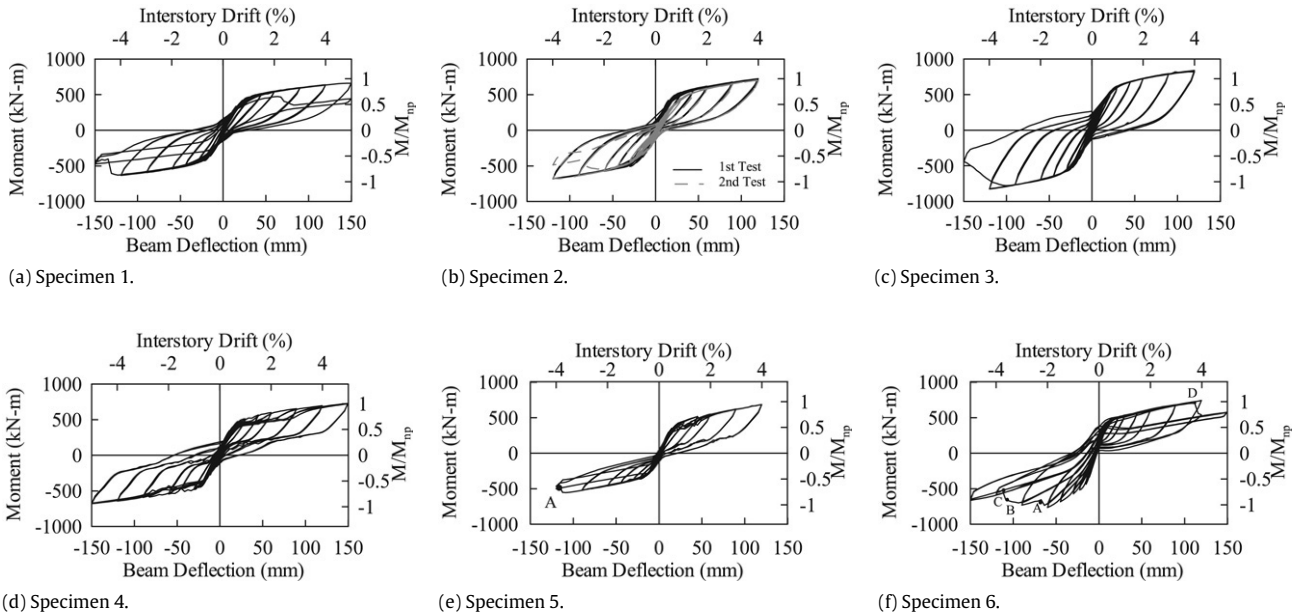
(f) Specimen 6.

Fig. 5. Moment versus beam deflection relationship.

Table 4
Experimental responses of connections

Specimen no.		1	2	3	4	5	6
$\frac{M_d}{M_{np}}$	$+^a$	0.44	0.43	0.57	0.47	0.41	0.56
	$-^b$	0.44	0.43	0.56	0.46	0.32	0.46
$\frac{M_{0.03}}{M_{np}}$	+	0.85	0.92	1.02	0.93	0.87	0.98
	−	0.85	0.91	0.97	0.94	0.77	0.97
Drift (%) at $\theta_g = 0.03$ rad.	+	3.8	3.8	4.0	3.9	3.4	3.3
	−	3.8	3.8	4.0	3.9	3.1	3.6

[a] Positive bending;
[b] Negative bending.

(a) Specimen 1 beam yielding (5% drift).
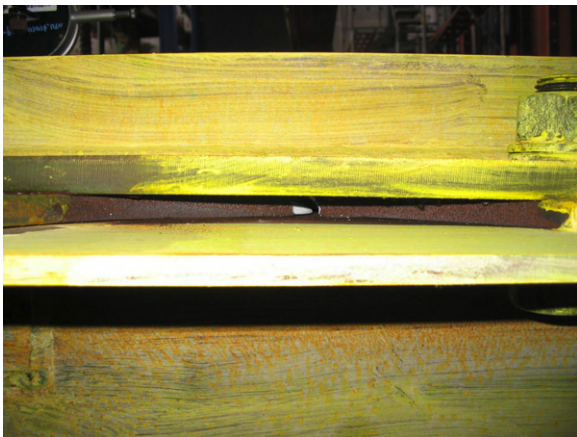
(b) Specimen 2 RFP fracture (4% drift, 2nd test).

Fig. 6. Observed performance for specimens 1 and 2.

(a) Specimen 3.

(b) Specimen 4.

Fig. 7. Beam deformation at an interstory drift of 5%.

4.2.2. Specimens 3 and 4

Beam yielding in Specimen 3 was visualized at an interstory drift of 1.5%. During subsequent loading, beam yielding accompanied by a high PT force resulted in larger residual deformation as compared to other specimens. In other words, small pinching of the hysteretic loops was observed [Fig. 5(c)]. The steel beam buckled at a second cycle of a 4% drift, corresponding to the gap-opening angle of 0.029 rad. (close to the predicted value of 0.03 rad.). Buckling became significant during the first cycle of a 5% drift [Fig. 7(a)], resulting in large strength degradation [Fig. 5(c)]. For Specimen 4, the beam flange near the end of the flange reinforcing plate yielded about an interstory drift of 2%, but beam buckling was hardly detected even at an interstory drift of 5% [Fig. 7(b)]. This drift value was corresponding to the gap-opening angle of 0.041 rad., which was much higher than the predicted value (0.032 rad.). The maximum strain in the beam flange was measured as 1.2% (= six times the yield strain) [Fig. 8(b)], significantly exceeding 1.4 times the yield strain in Specimen 3 [Fig. 8(a)].

### 4.2.3. Specimens 5 and 6

Specimen 5 used 4 and 8 mm thick top and bottom RFPs, respectively, leading to un-symmetrical responses [Fig. 5(e)]. The beam developed positive moments on the order of 16%–20% larger than negative moments. A reduction in the negative moment (marked as "A" in the figure) was due to a fracture of the top RFP in tension. Note that the fracture of the RFP in this specimen occurred earlier than that in Specimen 1 due to SS400 steel. This material has similar yield and tensile strengths as ASTM A36 steel (Table 3), but its elongation is 18% less than 28% of A36 steel.

The composite specimen showed a larger stiffness and moment as compared to the bare steel beam specimen. The composite specimen developed positive moments that ranged from 1%–8% larger than the bare steel beam specimen, and negative moments that ranged from 1%–63% larger than the bare steel beam specimen. Although the beam negative moments were much higher in the composite specimen than in the bare steel beam
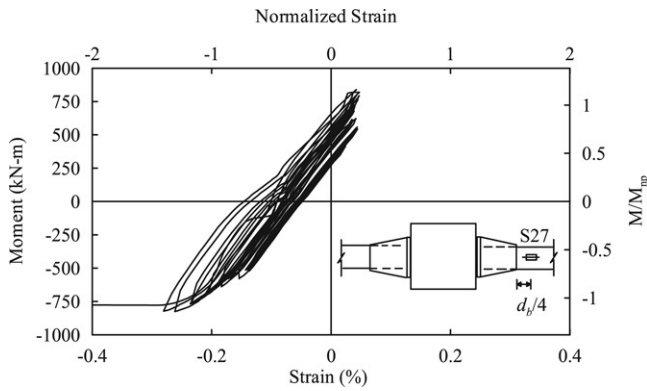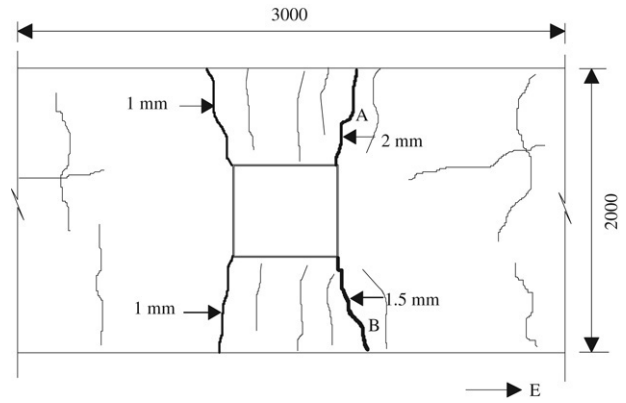
(a) Specimen 3.
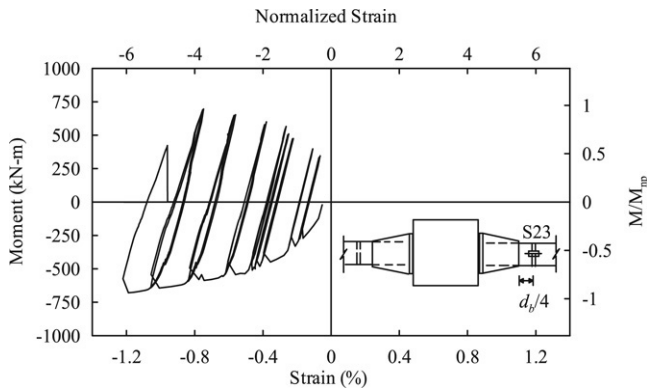
(b) Specimen 4.

Fig. 8. Moment versus beam flange strain relationship.

(a) 2% drift.

(b) 3% drift.

(c) 5% drift.

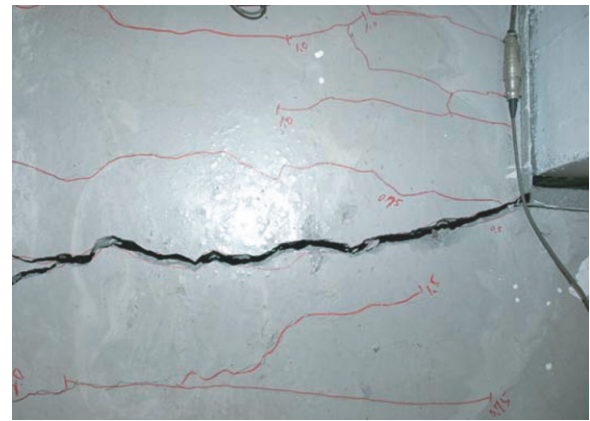**Fig. 9.** Slab crack (Specimen 6).

specimen, the beam positive and negative moments were similar in the composite specimen [Fig. 5(f)]. The re-centering hysteretic property also maintained for the beam under either positive bending or negative bending, suggesting that the proposed slab details are acceptable.

When the negative moments were attained in the composite specimen, the slab was generally cracked in a direction transverse to the beam. The first crack in the slab appeared midway of the beam soon after decompression. During subsequent loading, the number of cracks in a direction transverse to the beam increased. However, large cracks occurred near the beam-to-column interface as shown in Fig. 9(a). For example, when the east beam was under negative bending, the cracks, marked A and B in the figure, widened associated with opening at the east beam-to-column interface. The maximum crack width ranged from 1 to 2 mm at an interstory drift of 2%. Toward an interstory drift of −3%, the wire mesh, located on the north side of the composite slab, fractured along a crack "A", resulting in a slight reduction in the negative moment at step A [Fig. 5(f)]. A view of the column face is shown in Fig. 9(b); the crack width increased from 2 to 12 mm. Toward an interstory drift of −4%, the negative moment decreased again due to fractures of the wire mesh (step B), located on the south side of the slab, and fractures of the top RFP (step C). The bottom RFP fractured at a second cycle of an interstory drift of 4%, leading to a reduction in the positive moment at step D. The hysteretic responses at an interstory drift of 5% were then caused by the beam PT force and reinforcement tensile force. Fig. 9(c) shows an overall view of the composite slab at an interstory drift of 5%; all cracks except for the cracks near the beam-to-column interfaces are minimal. The cracks, extending from the beam-to-column interfaces, also closed after the test.
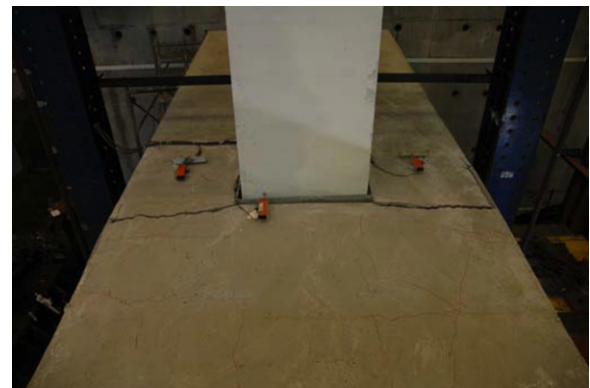
The gap-opening angle and the position of the neutral axis were measured by displacement transducers located along the depth of the beam at the beam-to-column interface. The gap-opening angles measured at different drifts are presented in Fig. 10(a). For Specimen 5, the top RFP is thinner than the bottom RFP, so the gap-opening angles in the beam under negative bending are larger than under positive bending. For the beam under negative bending, the gap-opening angles in the composite specimen are smaller than in the bare steel beam specimen because the tensile capacity of the slab inhibits a beam rotation. It also results in the negative neutral axis location nearer the beam top section, as compared to the bare steel beam specimen [Fig. 10(b)]. However, the positive gap-opening angles are similar in both specimens; the positive neutral axis locations are also similar in both specimens [Fig. 10(b)].

Fig. 11 shows moment-strain responses of the wire mesh, longitudinal bar, and metal deck near the beam-to-column
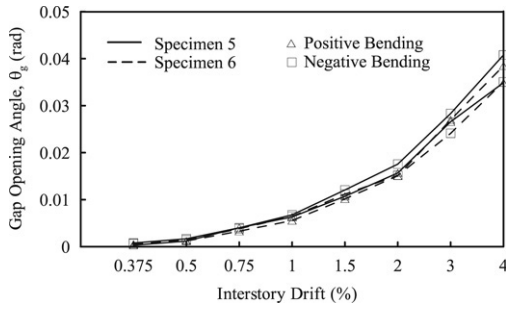
(a) Gap opening angle.
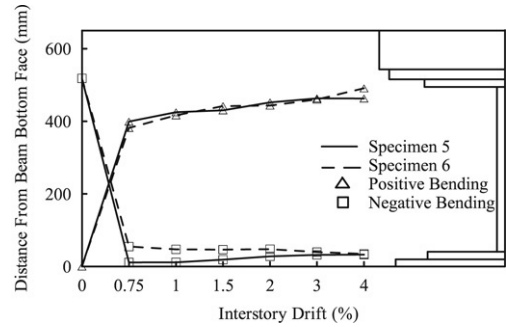
(b) Neutral axis location.

Fig. 10. Gap opening angle and neutral axis location for specimens 5 and 6.

(a) Wire mesh.

(b) Longitudinal bar.

(c) Metal deck.

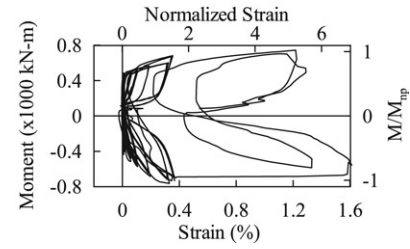**Fig. 11.** Moment-strain responses for wire mesh, longitudinal bar, and metal deck.

interface. The wire mesh, longitudinal bar, and metal deck are in tension for the beam under either positive bending or negative bending. A sudden strain increase in the longitudinal bar [Fig. 11(b)] corresponds to fractures of the wire mesh (at a 4% drift). Fig. 12 shows strain profiles along a longitudinal bar in the slab. Since the longitudinal bar has a 2000 mm debonded length through the connection, the strain is uniform within the debonded region before fractures of the wire mesh at a 4% drift.

## 5. Moment estimation for PT beams with a composite slab

The free-body diagram of the composite specimen (Fig. 13) was proposed to estimate moments contributed from each possible sources during the test. For beam positive and negative moments, the wire mesh, longitudinal reinforcement, and metal deck were in tension at the beam-to-column interface (Fig. 11), suggesting that tensile forces caused by the beam under negative bending are transferred to the other beam under positive bending. No separation between the metal deck and concrete was observed before fractures of the wire mesh, so perfect bonding could be assumed in transferring forces. For a specific drift during the test, the gap opening angle and the position of the neutral axis were obtained from Fig. 10. The RFP tensile and compressive forces, T_{RFP}, T'_{RFP}, C_{RFP}, and C'_{RFP}, were computed from deformations between the column face and the beam flange-RFP joint, and the axial force-deformation relationship of the RFP. The deformations were obtained by assuming a rigid-body rotation of the beam about the position of the neutral axis. The forces in the strands, T_u and T_l, were obtained from load cells. The forces in the wire mesh, T_{wire} and T'_{wire}, metal deck, T_{deck} and T'_{deck}, and longitudinal bars, T_{bar} and T'_{bar}, were calculated based on measured strains, material properties, and cross-sectional areas at the beam-to-column interface. Considering horizontal force equilibrium in each beam (Fig. 13), the compressive forces acting at the bearing plates, C_1 and C_2, could be determined. Note that the C_2 value was larger than the C_1 value because the bottom RFP was thicker than the top RFP. By summing the moments about the respective neutral axis
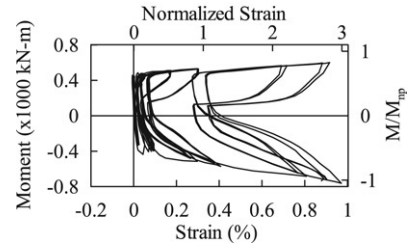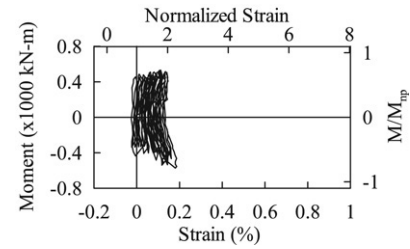
locations, c_1 and c_2, the respective negative and positive moments, M_1 and M_2, are:

$$
\begin{aligned}
M_1 = {} & \left[T_u \left(d'_{ST,u} \right) + T_l \left(d'_{ST,l} \right) + C_1 \left(\frac{2}{3} c_1 \right) \right. \\
& \left. + T'_{RFP} \left(d_t + \frac{t'_R}{2} - c_1 \right) + C'_{RFP} \left(c_1 + \frac{t_R}{2} \right) \right] \\
& + \left[T'_{bar} \left(d'_{bar} \right) + T'_{wire} \left(d'_w \right) + T'_{deck} \left(d'_d \right) \right]
\end{aligned}
\tag{5}
$$

$$
\begin{aligned}
M_2 = {} & \left[T_u \left(d_{ST,u} \right) + T_l \left(d_{ST,l} \right) + C_2 \left(\frac{2}{3} c_2 \right) \right. \\
& \left. + T_{RFP} \left(d_t + \frac{t_R}{2} - c_2 \right) + C_{RFP} \left(c_2 + \frac{t'_R}{2} \right) \right] \\
& - \left[T_{bar} \left(d_{bar} \right) + T_{wire} \left(d_w \right) + T_{deck} \left(d_d \right) \right]
\end{aligned}
\tag{6}
$$

where $d_{ST,u}$, $d_{ST,l}$, d_{bar}, d_w, and d_d are the distances from the position of the neutral axis, c_2 (for positive bending), to the upper strands, lower strands, reinforcement, wire mesh, and deck flute center, respectively. Notations $d'_{ST,u}$, $d'_{ST,l}$, d'_{bar}, d'_w, and d'_d are the distances from the position of the neutral axis, c_1 (for negative bending), to the upper strands, lower strands, reinforcement, wire mesh, and deck flute center, respectively. Notations t'_R and t_R are the top and bottom RFP thicknesses, respectively.

Fig. 14 shows the connection moments, which were calculated from the actuator forces times the distance to the beam-to-column interface, and the moments, which were calculated based on Eqs. (5) and (6) for the strands, RFPs, wire mesh, reinforcement, deck, and bearing plate. Some positive moments are below zero due to opposite contribution, as evident by the free-body diagram of the composite specimen (Fig. 13). The comparison was not made at a 3% drift because some strain gauges malfunctioned when the wire mesh fractured. Peak moments that sum each component
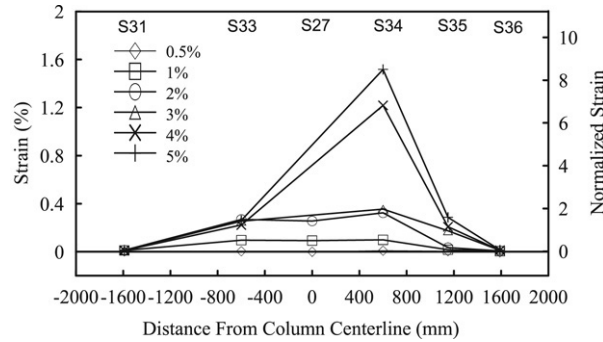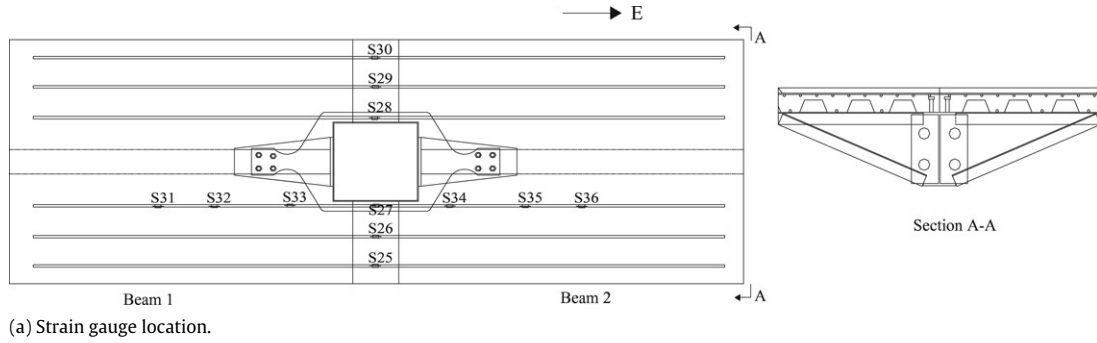
(a) Strain gauge location.

(b) Strain profiles.

Fig. 12. Strain profiles along a longitudianl bar (Specimen 6).
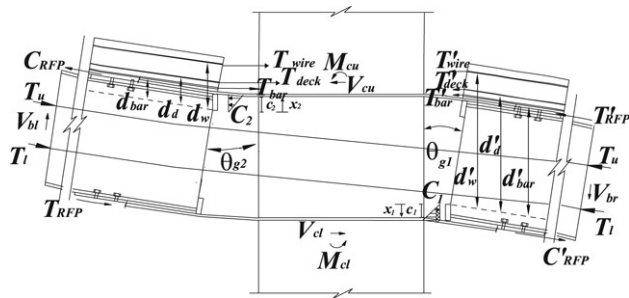
Fig. 13. Free-body diagram of a PT connection with slab.

(a) Positive bending.

(b) Negative bending.

Fig. 14. Moment comparison for each possible source.

contribution correlate reasonably with the moments calculated based on the actuator forces.

6. Summary of PT connection design procedure

The step-by-step design procedure for the PT connection with the RFPs is summarized as follows:

1. Select the target design drift (i.e. 4%, close to the gap-opening angle of 0.03 rad.), where the expected beam moment is M_b ($= \alpha M_{np}$, where $\alpha \approx 0.9$–1.0) and the expected moment provided by the RFPs is M_R ($= \beta M_{np}$, where $\beta \approx 0.2$–0.3).
2. Determine the area of strands based on the expected moment contributed by the strands, M_{ST} ($= \alpha M_{np} - \beta M_{np}$) using Eq. (2). It is suggested that the maximum strand stress remains below 0.8 times the yield strength of the steel.
3. To ensure full re-centering on load reversal, the RFP moment, M_R, must always be smaller than $M_{d,ST}$ ($=0.4$–$0.5M_{np}$), generated by the initial PT force, T_{in}, using Eq. (1).
4. Calculate the strand stress at the target gap-opening angle by considering the initial PT force (step 3), strand elongation, and beam shortening. If the calculated tensile stress is greater than the limit, it is suggested to increase the strand area in step 2.
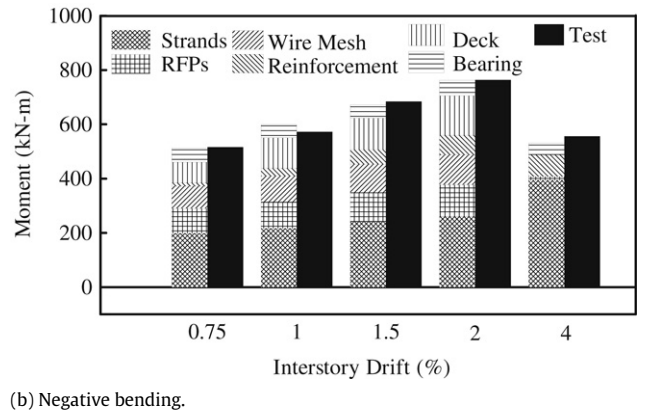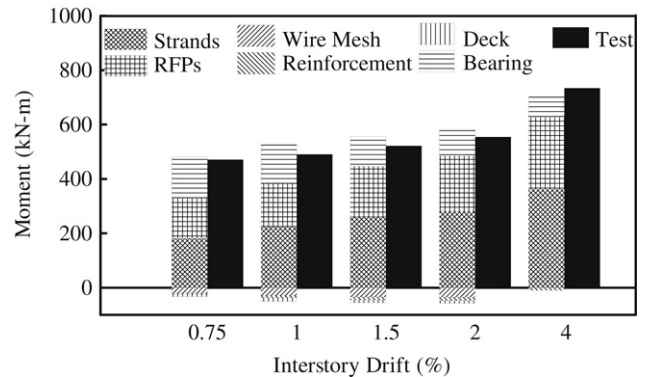
5. RFPs are then sized to provide moment βM_{np} based on the procedure in Chou et al. [7].

6. The flange reinforcing plate length is selected to limit the beam flange strain (where the flange reinforcing plates terminate in the beam) to the yield strain using Eq. (3). The flange reinforcing plate area should satisfy the criterion for yielding under bearing stresses at the beam-to-column interface.

7. The full-depth web stiffeners are introduced at a quarter of the beam depth from the end of the flange reinforcing plate to prevent beam local buckling when the beam is overloaded. The web stiffener thickness is equal to the beam web thickness.

8. For a metal deck with flutes running parallel to the PT beams, the metal deck is discontinuous at the column centerline and longitudinal bars include a debonded length to limit the maximum tensile strain less than 6-9 times the yield strain (Fig. 12) based on a rigid rotation of the bare steel beam. The cross-sectional area of the top RFP plus longitudinal bars within the effective slab width is close to that of the bottom RFP to provide similar positive and negative moments. The welded wire mesh could be used as in the steel moment-resisting frames.

7. Conclusions

Three series of six PT beam-to-column connections were tested under cyclic loading to evaluate the seismic behavior. The first test series was intended to examine the durability of the PT connection with RFPs. The second test series investigated the effects of flange reinforcing plates and of web stiffeners on beam local buckling. The third test series explored the influence of a composite slab on the connection re-centering behavior. Slab details, which included metal deck flutes, longitudinal bars, and wire mesh placed parallel to the beam, were intended to be representative of typical frame construction practice in Taiwan. To minimize moments contributed by the metal deck and longitudinal bars upon decompression, the metal deck was discontinuous at the column centerline and all bars had a 2000 mm debonded length near the connection region. The cross-sectional area of the top RFP plus longitudinal bars was nearly equal to that of the bottom RFP in order to achieve similar beam positive and negative moments. The experimental and analytical results of the three test series support the following conclusions:

1. The lengths of the flange reinforcing plates in Specimens 1 and 2 were determined based on the beam axial force and moment at the gap opening angle of 0.03 rad., which was 0.01 rad. higher than that adopted in the prior research [7]. Beam local buckling, noticed in the prior research, was not observed in Specimen 1 test at an interstory drift of 5%. Two cyclic tests conducted in Specimen 2 resulted in similar hysteretic responses before fractures of the RFPs. Note that the failure mode, rather than RFP buckling, was not observed in the prior research due to insufficient out-of-plane restraint to the RFP.

2. The lengths of the flange reinforcing plates in Specimens 3 and 4 were determined based on the beam axial force and moment at the gap opening angle of 0.01 rad. to evaluate the onset of beam local buckling. Beam yielding accompanied by a large PT force in Specimen 3 produced large residual drift and caused beam local buckling at an interstory drift of 4%. However, Specimen 4, which had two full-depth web stiffeners located near the end of the flange reinforcing plate, reached an additional 1% drift without beam buckling. The maximum strain in the beam flange was measured as 1.2% (=six times the yield strain), exceeding the strain of 0.28% (=1.4 times the yield strain) at the onset of beam buckling in Specimen 3.

3. Specimen 6 with a composite slab exhibited an increase in positive and negative moments on the order of 8 and 63% over the bare steel beam Specimen 5. The beam negative moment increase in the composite specimen increased residual deformations, but the re-centering characteristics were still maintained. The maximum beam positive and negative moments of the composite specimen were similar, less than the nominal moment capacity of the beam. It suggests that the proposed slab details are acceptable for the PT connection with metal deck flutes running parallel to the PT beam.

4. The proposed model considering a composite slab in the PT connection was able to explore moments contributed from the wire mesh, longitudinal reinforcement, and metal deck. Note that although the deck was separated along the column centerline, it still contributed to the connection moments before the wire mesh fractured. The wire mesh fractured at an interstory drift of 3%, leading to a separation between the deck and concrete and a reduction in the beam negative moments. Then, the cracks, extending from the beam-to-column interface, opened significantly for the beam under negative bending; other cracks were minimal. Note that all slab cracks closed after the test.

Although Specimen 4 reached an additional 1% drift compared to Specimen 3 at the ultimate response, web stiffener yielding and beam buckling were not observed in the test, indicating sufficient rigidity of the stiffeners to prevent buckling of the beam at a possible plastic hinge location. Future work is still needed for an optimal size of the web stiffener instead of just using the beam web thickness.

References

[1] Engelhardt MD. Design of reduced beam section moment connections. Proc., North American steel construction conference. Chicago: AISC; 1998. pp. 1–29.
[2] Uang CM, Yu QS, Noel S, Gross J. Cyclic testing of steel moment connections rehabilitated with RBS or welded haunch. J Struct Eng, ASCE 2000;126(1): 57–68.
[3] Kim T, Whittaker AS, Gilani ASJ, Bertero VV, Takhirov SM. Experimental evaluation of plate-reinforced steel moment-resisting connections. J Struct Eng, ASCE 2002;128(4):483–91.
[4] Ricles JM, Sause R, Peng SW, Lu LW. Excremental evaluation of earthquake resistant posttensioned steel connections. J Struct Eng, ASCE 2002;128(7): 850–9.
[5] Garlock MM, Ricles JM, Sause R. Experimental studies of full-scale posttensioned steel connections. J Struct Eng, ASCE 2005;131(3):438–48.
[6] Christopoulos C, Filiatrault A, Uang CM, Folz B. Posttensioned energy dissipating connections for moment-resisting steel frames. J Struct Eng, ASCE 2002;128(9):1111–20.
[7] Chou CC, Chen JH, Chen YC, Tsai KC. Evaluating performance of post-tensioned steel connections with strands and reduced flange plates. Earthq Eng Struct Dyn 2006;35(9):1167–85.
[8] Chou CC, Chen JH. Seismic behavior of steel beams post-tensioned to a reinforced concrete column with reduced flange plates. Report No. NSC 93-2625-Z-009-003, National Science Council, Taiwan, 2005.
[9] Chou CC, Tsai KC, Chen JH, Chen YC, Chuang SC. Cyclic behavior of post-tensioned steel connections with reduced flange plate and concrete slab. In: 1st international conference on advances in experimental structural engineering. 2005. p. 733–40.
[10] Wang YC. Effects of concrete slab on cyclic behavior of post-tensioned moment connections. Master thesis, advisor: Chou CC. Hsinchu (Taiwan): National Chiao Tung University; 2006.
[11] Timoshenko SP, Gere JM. Theory of elastic stability. New York: McGraw-Hill; 1963.
[12] ACI (American Concrete Institute) 318, Building code requirements for structural concrete and commentary, Farmington Hills, MI, 2002.
[13] FEMA (Federal Emergency Management Agency), Recommended seismic design criteria for new steel moment-frame buildings, Washington, DC. 2000.
[14] ASTM (American Society for Testing and Materials), Standard methods for tension testing of metallic materials, Designation No. E8-19, Philadelphia, 1997.
[15] AISC (American Institute of Steel Construction), Seismic provisions for structural steel buildings, Chicago, IL, 2002.